

## HEATING IN THE ACCRETED NEUTRON STAR OCEAN: IMPLICATIONS FOR SUPERBURST IGNITION

SANJIB GUPTA<sup>1</sup>, EDWARD F. BROWN, HENDRIK SCHATZ, PETER MÖLLER<sup>1</sup>, KARL-LUDWIG KRATZ<sup>2,3</sup>  
 Department of Physics and Astronomy, National Superconducting Cyclotron Laboratory, and Joint Institute for Nuclear Astrophysics,  
 Michigan State University, East Lansing, MI 48824; guptasanjib@lanl.gov, ebrown@pa.msu.edu,  
 schatz@nscl.msu.edu, moller@lanl.gov, klkratz@uni-mainz.de

*Draft version November 1, 2018*

### ABSTRACT

We perform a self-consistent calculation of the thermal structure in the crust of a superbursting neutron star. In particular, we follow the nucleosynthetic evolution of an accreted fluid element from its deposition into the atmosphere down to a depth where the electron Fermi energy is 20 MeV. We include temperature-dependent continuum electron capture rates and realistic sources of heat loss by thermal neutrino emission from the crust and core. We show that, in contrast to previous calculations, electron captures to excited states and subsequent  $\gamma$ -emission significantly reduce the local heat loss due to weak-interaction neutrinos. Depending on the initial composition these reactions release up to a factor of 10 times more heat at densities  $< 10^{11} \text{ g cm}^{-3}$  than obtained previously. This heating reduces the ignition depth of superbursts. In particular, it reduces the discrepancy noted by Cumming et al. between the temperatures needed for unstable  $^{12}\text{C}$  ignition on timescales consistent with observations and the reduction in crust temperature from Cooper pair neutrino emission.

*Subject headings:* dense matter — nuclear reactions, nucleosynthesis, abundances — stars: neutron—X-rays: binaries — X-rays: bursts

### 1. INTRODUCTION

The ability to regularly monitor the X-ray sky with instruments such as *RXTE* and *BeppoSAX* has produced many exciting discoveries in the last few years. An excellent example are superbursts (for a review see Kuulkers 2004). Like normal type I X-ray bursts (for a review, see Strohmayer & Bildsten 2004), superbursts are characterized by a rapid rise in the light curve followed by a quasi-exponential decay; when compared to type I X-ray bursts, superbursts are roughly  $\sim 10^3$  times more energetic, have cooling timescales of hours, and recur on timescales of years. For one source, 4U 1636–53, three superbursts have been observed over a span of 4.7 yr (Wijnands 2001; Kuulkers et al. 2004). Although most superbursts are observed at mass accretion rates  $0.1\text{--}0.3 \dot{M}_{\text{Edd}}$ , with  $\dot{M}_{\text{Edd}} \approx 10^{18} \text{ g s}^{-1}$  being the Eddington accretion rate, recently in ‘t Zand et al. (2004a) detected superbursts from the rapidly accreting source GX 17+2.

The currently favored scenario for these superbursts is the thermally unstable ignition of  $^{12}\text{C}$  at densities  $\sim 10^8\text{--}10^9 \text{ g cm}^{-3}$  (Cumming & Bildsten 2001; Strohmayer & Brown 2002). Cumming & Macbeth (2004) demonstrated that the superburst lightcurve after the peak luminosity has been reached declines as a broken power law, with the early behavior dependent on the burst energy and the later behavior dependent on the ignition depth. This behavior has been observed (Cumming et al. 2006). The ability to constrain the burst energetics and ignition depth is crucial, not only for understanding the ignition of  $^{12}\text{C}$  in a heavy-element bath, but also for probing the interior of the neutron star (Brown 2004; Cooper & Narayan 2005; Cumming et al. 2006). Brown (2004) demonstrated that the temperature at densities  $\sim 10^9 \text{ g cm}^{-3}$  is sensitive to the thermal conductivity

of the inner crust and the neutrino emissivity of the core; this was confirmed by Cooper & Narayan (2005) in a more extensive study. Recently, Cumming et al. (2006) showed that the neutrino emission from singlet-state Cooper pairing of neutrons in the inner crust limited the temperature at neutron drip to be  $\lesssim 5 \times 10^8 \text{ K}$ . Taken at face value, this would lead to superburst ignition column depths about an order of magnitude deeper than the  $0.5\text{--}3 \times 10^{12} \text{ g cm}^{-2}$  deduced from observations, and correspondingly to recurrence times that are about an order of magnitude longer than observed. This led Page & Cumming (2005) to speculate that the superbursters might in fact be strange stars.

The unstable ignition of  $^{12}\text{C}$  depends critically on the thermal structure of the outer crust and is sensitive to the heat sources located there. The outer crust of the neutron star is composed of nuclei and degenerate electrons and exists where the electron chemical potential  $\mu_e \lesssim 30 \text{ MeV}$  (see Pethick & Ravenhall 1998, for a lucid discussion). The ashes of hydrogen, helium, and carbon burning in the neutron star envelope are continuously compressed by the ongoing accretion of matter and incorporated into the crust. The increasing density induces nuclear reactions at various depths that can release energy. *We show that most of this energy is deposited in the crust, rather than being carried away by neutrinos. This leads to a hotter crust and decreases superburst ignition depths and recurrence times.*

Previous studies of the crust heat sources used a single representative isotope,  $^{56}\text{Fe}$  (Sato 1979; Haensel & Zdunik 1990) or  $^{106}\text{Pd}$  (Haensel & Zdunik 2003) for the product of H/He burning. Haensel & Zdunik (1990) found that electron captures would occur in two stages (see Fig. 1). The first electron capture (labeled “1” in Fig. 1) would occur when  $\mu_e \approx E_{\text{thr,gs-gs}}^{(Z,A)}$  for capture onto an even-even nucleus:  $(Z,A) + e^- \rightarrow (Z-1,A) + \bar{\nu}_e$ , where  $Z$  and  $A$  are even. Here the threshold is  $E_{\text{thr}} = E_{\text{thr,gs-gs}} + E_{\text{exc}}$ , where the threshold for the ground-state-to-ground-state transition  $E_{\text{thr,gs-gs}}$  is computed from atomic mass differences and therefore includes the

<sup>1</sup> Theoretical Division, Los Alamos National Laboratory, NM 87545

<sup>2</sup> Max-Planck-Institut für Chemie, Otto-Hahn-Institut, Joh.-J.-Becherweg 27, D-55128 Mainz, Germany

<sup>3</sup> HGF VISTARS, D-55128 Mainz, Germany

electron rest mass, and where  $E_{\text{exc}}$  is the energy of the lowest excited state into which the capture can proceed. Because of the odd-even staggering of the nuclear masses,  $E_{\text{thr,gs-gs}}^{(Z-1,A)}$  for electron capture onto the resulting odd-odd nucleus ( $Z-1, A$ ) is less than  $E_{\text{thr,gs-gs}}^{(Z,A)}$ . Consequently,  $\mu_e > E_{\text{thr,gs-gs}}^{(Z-1,A)}$  and a second electron capture  $(Z-1, A) + e^- \rightarrow (Z-2, A) + \bar{\nu}_e$  immediately follows. Where experimental data were lacking, which is the case for the vast majority of nuclei, the heat deposited into the crust  $Q$  was calculated assuming that the capture was into the ground state of the daughter nucleus (Fig. 1, label “4”). The heat deposited into the crust is then estimated as (Haensel & Zdunik 2003)  $Q = (\mu_e - E_{\text{thr,gs-gs}})/4$ , where the factor 1/4 arises from the integral over the reaction phase space in the limit that  $(\mu_e - E_{\text{thr}})/\mu_e \ll 1$ . This estimate assumes that final states are very low in excitation energy so that the contribution to the heat deposition from the radiative de-excitation of the daughter nucleus is always negligible compared to the heat release from the electron capture. In this picture, 75% of the nuclear energy release is emitted in form of neutrinos.

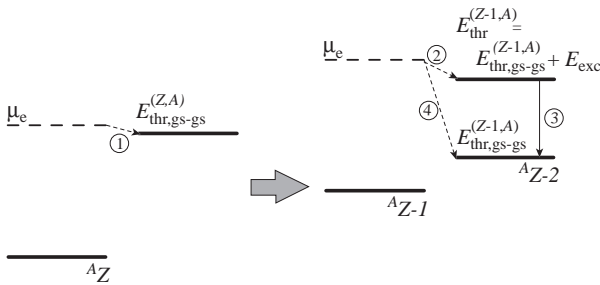


FIG. 1.— Electron capture for which the first transition (labeled “1”) proceeds to the ground state of nucleus  ${}^A Z - 1$ , but the second transition instead goes to an excited state “2” followed by a radiative de-excitation “3”. Previous works assumed that the second transition always went to the ground state “4”.

In this paper, we calculate heating from nuclear reactions in the outer crust (where the mass density is less than neutron drip,  $\sim 10^{11} \text{ g cm}^{-3}$ ) using realistic electron capture rates obtained by microscopic calculations of the transition matrix elements between the parent ground state and daughter excited states multiplied with the phase space factor corresponding to the  $Q$ -value of the decay. The rates depend on the excitation energy and the ambient temperature and density. We use a full reaction network having temperature- and density-dependences. Our thermal model of the crust, described in § 2, is coupled to the reaction network (§ 3), so that our solution is self-consistent. Instead of starting with a single nucleus, we follow the actual mix of nuclei initially produced by surface burning, both from the rp-process (§ 3.2.1) and a mixture in nuclear statistical equilibrium formed during a superburst (§ 3.2.2). We find that electron captures deposit considerably more energy in the crust than in previous estimates (Haensel & Zdunik 2003). This larger heat deposition is mainly due to the electron captures populating excited states with energy  $E_{\text{exc}}$  (Fig. 1, label “2”), rather than capturing into the ground state as assumed previously. The populated excited states then radiatively de-excite (Fig. 1, label “3”), depositing the entire excitation energy as heat into the crust. We also introduce an approximate model that gives a good esti-

mate of the heating in the outer regions of the crust for an arbitrary mixture in § 3.3 and describe the implications for superburst ignition in § 4.

## 2. THE THERMAL STRUCTURE OF THE CRUST

Our thermal model is the same as used by Brown (2000, 2004) and we shall only summarize its essential properties here. Over the crust, the gravitational potential  $\Phi \approx \frac{1}{2}c^2 \ln(1 - 2GM/rc^2)$  is nearly constant; moreover, we are always in hydrostatic equilibrium and can approximate the pressure as being nearly independent of temperature. Under these approximations, we then solve the equations for temperature, luminosity, and nuclear heating,

$$e^{-\Phi/c^2} \frac{d(e^{\Phi/c^2} T)}{dr} = -\frac{L(1+z)}{4\pi r^2 K} \quad (1)$$

$$e^{-2\Phi/c^2} \frac{d(e^{2\Phi/c^2} L)}{dr} = \frac{dL_{\text{nuc}}}{dr} - 4\pi r^2 (1+z) \epsilon_{\nu}, \quad (2)$$

$$\frac{dL_{\text{nuc}}}{dr} = \dot{M} Q(r) m_{\text{u}}^{-1} \quad (3)$$

where  $z = (1 - 2GM/rc^2)^{-1/2} - 1$  is the gravitational redshift,  $Q(r)$  is the heat deposited per accreted nucleon as computed from our reaction network (§ 3), and  $m_{\text{u}} = 1.66 \times 10^{-24} \text{ g} = 1 \text{ u}$ . Over the crust the potential  $\Phi$  varies only slightly and our code simplifies equations (1) and (2) by holding  $e^{\Phi/c^2}$  constant.

We model the core with an analytical density prescription  $\rho = \rho_0 [1 - (r/R)^2]$  (Tolman 1939), where  $\rho_0 = 15(8\pi)^{-1} M R^{-3}$  with  $R = (2GM/c^2) [1 - (1+z)^{-2}]^{-1/2}$ . Here  $r$  and  $R$  are respectively the circumferential radial coordinate and stellar radius. This prescription gives a reasonable approximation to the  $\rho(r)$  that would be obtained from a modern nuclear equation of state (EOS) (see Lattimer & Prakash 2001, and references therein). With this choice for the EOS, the gravitational mass of the neutron star  $M$  and redshift  $z$  specify the mechanical structure of the star. We choose the crust-core boundary to be at a transition density  $1.6 \times 10^{14} \text{ g cm}^{-3}$ , which is the density found by a Maxwell construction using an EOS for the inner crust (Negele & Vautherin 1973) and the core EOS (Akmal et al. 1998). We then adopt a neutron star of mass  $1.6 M_{\odot}$ , and set the radius at the crust-core boundary to 10.5 km. This choice makes  $[1 - 2GM/(rc^2)]^{-1/2} = 1.35$  at the boundary. Our neutron star then has a radius 10.8 km and a surface gravity  $2.43 \times 10^{14} \text{ cm s}^{-2}$ .

For our numerical calculations we use an accretion rate, measured in the rest frame at the surface, of  $\dot{M} = 3.0 \times 10^{17} \text{ g s}^{-1}$ ; the local accretion rate, per unit area, is then  $2.1 \times 10^4 \text{ g s}^{-1} \text{ cm}^{-2}$  and the luminosity (for spherical accretion) is 0.3 of the Eddington luminosity for a solar composition<sup>4</sup>. The core neutrino emissivity is modified Urca with an emissivity  $10^{20} (T/10^9 \text{ K})^8 \text{ erg cm}^{-3} \text{ s}^{-1}$ . Note that because our starting density for the integration is  $\rho = 6.2 \times 10^6 \text{ g cm}^{-3}$ , which is just below where the rp-process burning has concluded, we do not resolve the H/He burning shell in the envelope. Observations of the ratio of persistent fluence to burst fluence

<sup>4</sup> Here  $\dot{M}$  is the baryon accretion rate expressed in mass units, and not the rate at which the gravitational mass of the star changes

suggest that a good fraction of the accreted H/He burns stably (in 't Zand et al. 2004b), so we set the temperature at this boundary to be  $4.2 \times 10^8$  K, which is computed by integrating steady H burning (Schatz et al. 1999) at a local accretion rate of  $\dot{m} = 2.6 \times 10^4 \text{ g s}^{-1} \text{ cm}^{-2}$ .

Solving equations (1) and (2) requires the EOS, thermal conductivity  $K$  and neutrino emissivity  $\varepsilon_\nu$ . We use a tabulated electron EOS (Timmes & Swesty 2000) with ion electrostatic interactions (Farouki & Hamaguchi 1993). The pressure of the free neutrons is computed using a zero-temperature compressible liquid-drop model (Mackie & Baym 1977). Heat is transported by degenerate, relativistic electrons; our treatment of the electron scattering frequency follows Brown et al. (2002) and Brown (2004) and we presume that the crust has a completely disordered lattice (Jones 2004) so that the heat transport is controlled by electron-impurity scattering (Itoh & Kohyama 1993).

Our neutrino emissivity in the crust,  $\varepsilon_\nu$ , includes contributions from bremsstrahlung (Haensel et al. 1996) and Cooper pairing of neutrons in the  $^1S_0$  state (Yakovlev et al. 1999) in the inner crust. Our treatment of neutrino-antineutrino bremsstrahlung uses a Coulomb logarithm appropriate for a liquid and does not include band-structure effects (Pethick & Thorsson 1994; Kaminker et al. 1999), which is consistent with our assumption that the lattice is completely disordered. In the outer crust we have neglected the plasmon neutrino emissivity (Itoh et al. 1996), which is actually the dominant mode of neutrino emission there. At the temperatures of interest, however, the neutrino emission from the outer crust is negligible.

The dominant coolant in the crust is the neutrino emission from paired neutrons in the inner crust. For the critical temperature  $T_c$  of the paired neutrons, we choose a Gaussian in neutron Fermi momentum  $k_F$  with a maximum  $\max(k_B T_c) = 0.8 \text{ MeV}$  at  $k_F = 0.8 \text{ fm}^{-1}$ , and a width  $0.28 \text{ fm}^{-1}$ . These parameters are chosen to reproduce closely the  $T_c(k_F)$  of Ainsworth et al. (1989). As shown by Cumming et al. (2006), the strong temperature sensitivity of the neutrino emissivity  $\varepsilon_\nu^C$  makes the crust temperature rather insensitive to the precise dependence of the critical temperature on density.

Recently, Leinson & Perez (2006) argued that vertex corrections in the expansion of the singlet-state interaction would reduce  $\varepsilon_\nu^C$  by a large factor  $\sim (v_F/c)^4 \ll 1$ , where  $v_F$  is the neutron Fermi velocity. Sedrakian et al. (2006) argued that although the vertex corrections would change the temperature dependence of  $\varepsilon_\nu^C$ , the reduction would only be of order unity. We use for  $\varepsilon_\nu^C$  the rate from Yakovlev et al. (1999), but we will include, in § 4, a calculation with this emission suppressed to demonstrate how the ignition depth remains sensitive to  $\varepsilon_\nu^C$ .

We couple the steady-state thermal equations (1)–(3) with the reaction network calculations (§ 3.1) via an iterative procedure. Starting from an initial choice for the temperature profile  $T(r)$ , we integrate the reaction network along the path  $\{T[t(r)], \rho[t(r)]\}$ , where  $t$  refers to the Lagrangian time since the fluid element was deposited onto the star; in our plane-parallel approximation,  $t(r) = y(r)/\dot{m}$ , with  $y \approx P/g$  being the column depth. For the convenience of the reader, we show, in Figure 2, the column and mass density as a function of electron chemical potential  $\mu_e$  in the outer crust composed of rp-process ashes (§ 3.2.1). The curves obey the relation  $\mu_e \propto (\rho Y_e)^{1/3} \propto y^{1/4}$ , where  $Y_e$  is the electron abundance. For future reference, we also plot in Figure 2 the electron plasma

frequency (*dashed line*), which scales with electron chemical potential as  $\hbar\omega_{p,e} \approx 78 \text{ keV} (\mu_e/1 \text{ MeV})^{3/2}$ . For comparison, the thermal energies are  $k_B T = 43 \text{ keV} (T/5 \times 10^8 \text{ K}) < \hbar\omega_{p,e}$  throughout much of the crust. Our reaction network does not account for this large  $\hbar\omega_{p,e}$  in computing  $(\gamma, n)$  rates. We therefore stop the integration at  $\mu_e = 20 \text{ MeV}$  ( $\rho \gtrsim 2 \times 10^{11} \text{ g cm}^{-3}$ ) where the neutron abundance begins to rise steeply. The neutrons are not yet in  $\beta$ -equilibrium at this point, and the density is still less than neutron drip.

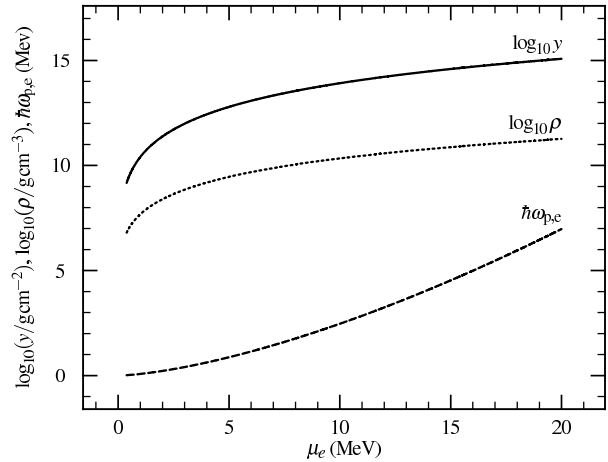


FIG. 2.— Column density  $y = P/g$  (solid line), mass density  $\rho$  (dotted line), and electron plasma frequency  $\hbar\omega_{p,e}$  (dashed line) as a function of electron chemical potential  $\mu_e$  in the outer crust where  $\mu_e < 20 \text{ MeV}$ . The column  $y$  is for a neutron star of mass  $1.6 M_\odot$  and radius  $10.8 \text{ km}$ .

The output of the reaction network gives us the local heat  $Q(r)$  deposited in the shell  $\{r, r + \Delta r\}$  per accreted nucleon. We use  $Q(r)$  and the abundance vector  $\vec{Y}(r)$  to solve equations (1)–(3) and construct a new thermal profile. For the inner crust we use the composition and heating from Haensel & Zdunik (2003)<sup>5</sup>. We then use the resulting thermal profile to update the network calculation, and we repeat this process until the thermal profile has converged. Typically only a few iterations are required, as the heating from electron captures is insensitive to the crust temperature.

### 3. NUCLEAR REACTIONS IN THE OUTER CRUST

The evolution of the composition and the associated nuclear energy generation, which produces the flux in the crust (eq. [2]–[3]), is calculated with a nuclear reaction network of  $\approx 1500$  isotopes covering the mass range  $A = 1$ –106 and extending from proton-rich rp-process ashes to the neutron dripline. In this section, we first describe how the electron capture and  $\beta$ -decay rates are calculated. We next describe the heating in the outer crust with two different initial compositions: rp-process and superburst ashes. Building on these results, we then develop a method to approximate the heating in the outer crust for an arbitrary composition.

#### 3.1. The Nuclear Model

We calculate electron capture rates for each time step of the integration of the reaction network using a table of electron

<sup>5</sup> The focus of this paper is how the thermal profile, and in particular the ignition depth of  $^{12}\text{C}$ , changes when the additional nuclear physics is added to the outer crust. An exploration of the reactions in the inner crust is left for future work.

capture transition strengths as a function of excitation energy in the daughter nucleus and a fast analytic phase space approximation (Becerril Reyes et al. 2006) that is valid for low temperatures. This phase space calculation takes into account the temperature and density dependence of the electron capture rates and is accurate enough to handle the sharp reaction thresholds that make table interpolation impossible. Temperatures and densities are calculated self-consistently from the energy generation and composition determined by the reaction network using an iterative procedure with the thermal model discussed in § 2.

Our nuclear model used to calculate the transition strength functions is described in detail in Möller & Randrup (1990) and here we just give a summary of its properties. We consider only allowed Gamow-Teller transition strength, which is computed in the quasi-particle random-phase approximation (QRPA). To obtain the wave functions we solve the Schrödinger equation for a deformed folded-Yukawa single-particle potential. We then add pairing and Gamow-Teller residual interactions treated in the Lipkin-Nogami and random phase approximations. Ground-state deformation parameters and masses are obtained from the finite-range droplet model (Möller et al. 1995). We calculate neutrino losses for each transition, rather than assuming that a fixed fraction of  $(\mu_e - E_{\text{thr}})$  is lost to neutrinos. As temperatures are low and radiative de-excitation timescales are much faster than weak interaction timescales, we assume that the parent nuclei are in their ground states.

For the depths considered in this calculation, electron-capture-induced neutron emission is not important. We further assume that  $\beta^-$  decay is always completely blocked. This is a good assumption in most cases as temperatures are low, and because most electron captures either proceed in a double step, with the second step proceeding with  $\mu_e \gg E_{\text{thr,gs-gs}}$ , or, if they occur at threshold, populate excited states in the final nucleus. In both cases,  $\mu_e$  is much larger than the  $\beta^-$  decay  $Q$ -value, which is always equal or less than the ground state to ground state electron capture threshold. We will discuss some possible exceptions to this in § 3.2.1.

While our main goal is to explore the crust heating within the framework of electron capture rates computed from the QRPA strength functions, we did adjust the transition energies in one case, for which the QRPA predictions are at odds with experimental information, and for which this has a strong effect on the crustal heating. Our model predicts that the electron capture on  $^{104}\text{Rh}$  proceeds to an excited state at 5.3 MeV, which would result in strong heating at that depth. Experimental data (Frevert et al. 1965) shows, however, that while  $^{104}\text{Rh}$  is  $\beta^-$  unstable, it also has a small ground-state-to-ground-state electron capture branch with a positive  $Q$ -value. As a result there is no nuclear excitation energy released and the heat deposition from this reaction is much smaller than predicted from our model.

In addition to the weak interaction rates, our network includes neutron capture rates, calculated with the statistical Hauser-Feshbach code NON-SMOKER (Rauscher & Thielemann 2000). The corresponding  $(\gamma, n)$  rates are calculated from detailed balance. For consistency we use the NON-SMOKER rates based on masses predicted by the finite-range droplet model. For the conditions considered here the neutrons are always non-degenerate; denoting the degeneracy by  $\eta = \mu_n (k_B T)^{-1}$ , we require for degeneracy an

abundance

$$Y_n > 0.015 \left( \eta \frac{T}{10^9 \text{ K}} \right)^{3/2} \left( \frac{10^{12} \text{ g cm}^{-3}}{\rho} \right). \quad (4)$$

For typical values  $T = 5 \times 10^8 \text{ K}$ ,  $\rho = 2 \times 10^{11} \text{ g cm}^{-3}$ , and taking  $\eta = 0.1$  as a fiducial threshold, we have  $Y_n > 8.4 \times 10^{-4}$  as the abundance threshold beyond which neutron degeneracy becomes important. At the densities we consider, the neutron abundance is well below this threshold. Our theoretical  $(n, \gamma)$  and  $(\gamma, n)$  rates do not account for the suppression of photons below an energy of  $\hbar\omega_{p,e}$  in a dense plasma. Where the neutron separation energies  $S_n > \hbar\omega_{p,e}$  this does not lead to a large correction in the rate. As we show in § 3.2.1, at  $\mu_e \gtrsim 14 \text{ MeV}$  some of the nuclei present have sufficiently low  $S_n$  that  $(\gamma, n)$  reactions would occur if the photodisintegration rates were not suppressed. A calculation of the  $(\gamma, n)$  and  $(n, \gamma)$  rates in this regime is outside the scope of this paper; for now, we will indicate their possible impact with the recognition that a more careful treatment of these reaction rates is warranted.

The output of the reaction network is the crust composition and heat deposition  $dQ = dE_{\text{nuc}} + dE_e - dE_\nu$  for each timestep  $dt = (\rho/\dot{m})dr$ . Here  $dE = \sum_i dY_i BE_i$  is the nuclear energy generation calculated from the abundance change  $dY_i$  and binding energy  $BE_i$  of each isotope  $i$ ,  $dE_e = \mu_e dY_e$  is the energy change due to changes in electron abundance, and  $dE_\nu$  is the energy released as neutrinos from electron capture. Here all heat depositions are per unit mass. Thermal neutrino losses, i.e., neutrino-pair bremsstrahlung and Cooper-pair neutrino emission, are included as cooling terms  $\epsilon_\nu$  in the thermal calculation (cf. § 2). We neglect the contribution from the change in Coulomb lattice energy  $dE_{\text{lat}}$  arising from the change in nuclear charge during an electron capture. Consider a single ion species  $(Z, A)$  with number density  $n_{\text{ion}}$ . The lattice energy is mostly due to the Madelung term,  $E_{\text{lat}} \approx -0.9(n_{\text{ion}}/\rho)k_B T \Gamma$ , where  $\Gamma = (Ze)^2/(ak_B T)$  and  $a$  is the ion sphere radius. The ratio of the lattice energy to electron energy is therefore  $\propto \alpha Z^{2/3}$ , where  $\alpha = e^2/\hbar c$ ; with the numerical coefficients inserted this ratio is  $\approx 3 \times 10^{-3} Z^{2/3} \ll 1$  throughout the outer crust. As a result, the shift in the location of the transitions is small. Moreover, for a two-step electron capture, the contribution to  $dQ$  comes from the *difference* in  $dE_{\text{lat}}$  between the two transitions, i.e., in the relative shift of the two transitions. This difference contributes  $\approx 76 \text{ keV u}^{-1} (\rho/10^{10} \text{ g cm}^{-3})^{1/3} A^{-4/3} \lesssim 1 \text{ keV u}^{-1}$  for the cases we consider here.

### 3.2. Heat Sources in the Outer Crust

Using the model described above, we computed the heat release for different starting compositions. In the following discussions, we highlight the dominant transitions in each.

#### 3.2.1. rp-Process Ashes

We first calculate the heat sources in the outer crust using rp-process ashes from a one-zone X-ray burst model (Schatz et al. 2001). The peak of the nuclide distribution is around  $A = 104$ , and it is useful to compare our results with those of Haensel & Zdunik (2003), who started with a single nuclide,  $^{106}\text{Pd}$ . The initial composition is dominated by  $^{104}\text{Cd}$  (25% by mass),  $^{105}\text{Cd}$  (9.6% by mass), and  $^{68}\text{Ge}$  (7.1% by mass). Other mass chains with mass fractions above 2% are  $A = 64, 72, 76, 98, 103, \text{ and } 106$ . There are also some small

residual amounts of  $^{12}\text{C}$  (0.7% by mass) and  $^4\text{He}$  (0.5% by mass). Figure 3 displays  $\langle Z \rangle$  (lower solid line) and  $\langle A \rangle$  (upper solid line) for this mixture as a function of  $\mu_e$ . The rms deviations about  $\langle Z \rangle$  and  $\langle A \rangle$  are indicated (shaded bands) as well. For comparison, we also plot the  $Z$  and  $A$  (dashed lines) from Haensel & Zdunik (2003). As the fluid element chemical potential increases beyond  $\mu_e = 4$  MeV,  $^{12}\text{C}$  fuses into heavier elements, with carbon being depleted by 90% at  $\mu_e = 5.8$  MeV ( $\rho = 4.5 \times 10^9 \text{ g cm}^{-3}$ ). This leads to the rise in  $\langle A \rangle$  shown in Figure 3. The abundances of  $^{12}\text{C}$  is so small, however, that they contribute a negligible amount of heating at these shallow depths.

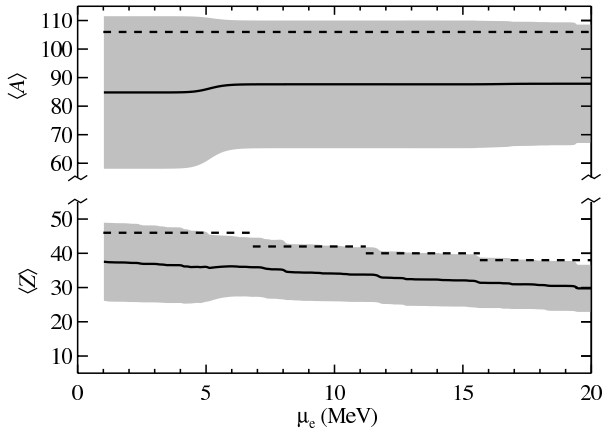


FIG. 3.— Composition ( $\langle Z \rangle$  and  $\langle A \rangle$ ; solid lines) for the compression of the rp-process ashes from X-ray bursts. We show the rms deviation about  $\langle Z \rangle$  and  $\langle A \rangle$  (shaded bands) for this distribution of nuclides. For comparison we also show the  $Z$  and  $A$  for the composition used by Haensel & Zdunik (2003, dashed lines).

We start our calculation at  $\mu_e = 0.38$  MeV ( $\rho = 6.2 \times 10^6 \text{ g cm}^{-3}$ ). There is an initial spike in heating as the fluid element comes into  $\beta$ -equilibrium. This heating is an artifact of our calculation, but, being located at the outer boundary where  $T$  is fixed, does not affect the resulting thermal profile. As the fluid element is moved to greater depth, the rising  $\mu_e$  induces electron captures that reduce  $\langle Z \rangle$  while preserving  $\langle A \rangle$  (Fig. 3). For  $\mu_e \gtrsim 14$  MeV ( $\rho \gtrsim 6 \times 10^{10} \text{ g cm}^{-3}$ ),  $\langle A \rangle$  is no longer constant, as  $(\gamma, n)$  and  $(n, \gamma)$  reactions alter the relative abundance of different mass chains. Figure 4 shows the integrated deposited energy (solid line) as a function of  $\mu_e$ . In this plot we set the integrated heat release to zero at  $\mu_e = 1.0$  MeV so that we can compare our results to those of Haensel & Zdunik (2003, dashed line). In the range  $1 \text{ MeV} < \mu_e < 14 \text{ MeV}$ , electron captures deposit  $66.3 \text{ keV u}^{-1}$ , which considerably exceeds the previous estimate of  $16.9 \text{ keV u}^{-1}$  (Haensel & Zdunik 2003). In this range of  $\mu_e$ , neutrinos carry away  $37.2 \text{ keV u}^{-1}$ .

This much larger heat deposition is due to our use of realistic electron capture rates, which often lead to the population of excited states in the daughter nucleus rather than the daughter ground state as assumed previously. Electron capture thresholds are therefore increased by these excitation energies. More importantly, however, the radiative de-excitation of the excited state deposits the excitation energy as heat, rather than having it carried off by neutrinos. Note that the sum of the heat deposited in the crust and the neutrino loss is  $83.3 \text{ keV u}^{-1}$ , which is only slightly larger than the comparable total heat for the calculation of Haensel & Zdunik (2003),

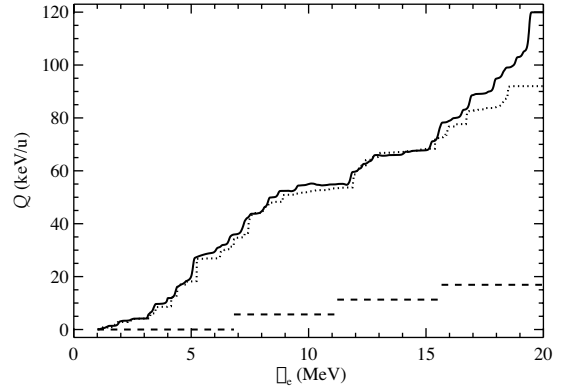


FIG. 4.— Integrated heat release in the crust from the compression of the rp-process ashes from X-ray bursts (solid line). For comparison, we also show (dashed line) the integrated heat released in the model of Haensel & Zdunik (2003), as well as the results from our approximate model (dotted lines, see § 3.3).

where a single mass  $A = 106$  was used.

Therefore, electron captures on even-even, odd-even, or even-odd nuclei, which tend to occur where the  $\mu_e = E_{\text{thr}}$ , can now deposit considerable amounts of heat. These reactions were not considered as heat sources before, as it was assumed that they proceeded from ground state to ground state. In addition, for the electron captures on the odd-odd nuclei—the main heat sources in previous work—the fraction of energy lost to neutrinos is considerably reduced.

As an example, a prominent heat source that can be identified in Figure 4 is the two step electron capture transition of  $^{104}\text{Ru}$  into  $^{104}\text{Mo}$  at  $\mu_e = 5.2$  MeV. The electron capture on  $^{104}\text{Ru}$  has a threshold for the transition into the daughter ground state of  $E_{\text{thr,gs-gs}} = 5.09$  MeV and is predicted to proceed to a low-lying state in  $^{104}\text{Tc}$  at  $E_{\text{exc}} = 0.15$  MeV. Therefore, this transition occurs at  $\mu_e \approx E_{\text{thr,gs-gs}} + E_{\text{exc}} = 5.24$  MeV. The subsequent electron capture on  $^{104}\text{Tc}$  has a lower ground state to ground state threshold  $E_{\text{thr,gs-gs}} = 1.96$  MeV and is dominated by a transition to an excitation energy of  $E_{\text{exc}} = 2.80$  MeV in  $^{104}\text{Mo}$ . For the latter transition, about 75% of the transition energy  $\mu_e - E_{\text{thr,gs-gs}} - E_{\text{exc}} = 0.48$  MeV is lost to neutrinos, but the entire excitation energy  $E_{\text{exc}}$  for both steps is deposited as heat, resulting in a total heat deposition of  $Q = 3.07$  MeV per transition. The heat generated per accreted nucleon is then  $QY_{104} = 8.6 \text{ keV u}^{-1}$ , with  $Y_{104} = 2.8 \times 10^{-3}$  being the abundance in the  $A = 104$  chain. If the electron capture on  $^{104}\text{Tc}$  proceeded through the ground state of  $^{104}\text{Mo}$ , as assumed in previous works, then about 75% of the entire transition energy  $\mu_e - E_{\text{thr,gs-gs}} = 3.28$  MeV would be lost to neutrinos and the heat deposition would be reduced by a factor of 3.6 to about  $0.82$  MeV per transition. Another prominent heat source in the region  $\mu_e \lesssim 14$  MeV is the two-step electron capture on  $^{68}\text{Fe}$  at  $\mu_e \approx 11.8$  MeV (with heat deposition  $QY_{68} = 5 \text{ keV u}^{-1}$ ).

Typically, transitions in even- $A$  chains, such as the electron capture on  $^{104}\text{Ru}$  discussed above, occur as double steps due to the odd-even staggering of the electron capture thresholds, although exceptions can occur if the transitions populate high lying excited states. In contrast, thresholds in odd- $A$  chains tend to increase steadily with electron captures proceeding in single steps. However, there are also some important two-step electron captures in odd mass chains, most importantly the

transition from  $^{105}\text{Rh}$  into  $^{105}\text{Tc}$  at  $\mu_e = 4.4$  MeV. While the electron capture on  $^{105}\text{Rh}$  has a ground-state-to-ground-state threshold of 1.6 MeV, the transition is predicted to mainly go to a 2.9 MeV excited state in  $^{105}\text{Ru}$ . This effectively raises the threshold to  $\approx 4.5$  MeV. Therefore, even though the electron capture on  $^{105}\text{Rh}$  occurs at an  $\mu_e$  near this “effective” threshold, the full 2.9 MeV excitation energy is deposited into the crust. Following the electron capture onto  $^{105}\text{Rh}$ ,  $\mu_e$  is then sufficient to overcome the 3.6 MeV threshold (which includes a final state excitation energy of 0.15 MeV) for electron capture  $^{105}\text{Ru} \rightarrow ^{105}\text{Tc}$ . In total this sequence deposits  $3.8 \text{ keV u}^{-1}$  into the crust ( $Y_{105} = 1.3 \times 10^{-3}$ ).

The mass chains  $A = 72, 76, 98,$  and  $103$  also contribute  $2\text{--}3 \text{ keV u}^{-1}$  each in the region  $\mu_e < 14$  MeV. In total, there are about 15 transitions that generate  $2 \text{ keV u}^{-1}$  or more and that are responsible for about 66% of the total deposited heat. The remainder of the heating is produced by a larger number of less energetic electron captures. At  $\mu_e \gtrsim 14$  MeV, we begin to see captures of neutrons liberated by  $(\gamma, n)$  reactions on nuclei with low  $S_n$ , such as  $^{103}\text{Kr}$  ( $S_n = 1.9$  MeV). As explained in § 3.1, the  $(\gamma, n)$  rates are strongly suppressed where  $S_n < \hbar\omega_{p,e}$  by the absence of photons with  $\omega < \omega_{p,e}$  and so the reactions we see are probably an artifact of our network. It is interesting to note, however, that in a crust composed of a mix of a number of different nuclei with different mass numbers, the neutrons released by nuclei with low  $S_n$  tend to be recaptured quickly by nuclei with larger neutron capture  $Q$ -values. It is only at a larger depth, where most  $A$ -chains have reached low  $S_n$ , that an appreciable neutron abundance would begin to appear.

Figure 5 (*solid lines*) demonstrates the effect on the thermal structure of the crust by the heating from all of the reactions described above. Plotted are the temperature, in units of  $10^9$  K (*top*), and the luminosity  $L$  (*bottom*), which is multiplied by  $m_u/\bar{M}$  so that it is in units of MeV. For comparison, we also show (*dotted lines*) the thermal profiles obtained using the composition and heating of Haensel & Zdunik (2003). The crust temperature is clearly elevated in the outer crust.

An effect that we have not included in our calculations explicitly and that could in principle lead to additional cooling is an Urca process that might occur for single-step, ground-state-to-ground-state electron captures, when the subsequent electron capture is blocked until significantly higher density. If the temperature is sufficiently high for such an electron capture to occur pre-threshold, the reverse  $\beta^-$  decay is not blocked. Until  $\mu_e$  has risen to a sufficiently large value the electron capture occurs in tandem with a ground-state-to-ground-state  $\beta^-$  decay in the reverse direction and an Urca process will result. While such transitions are rare (most electron captures proceed as double steps, or to excited states) there are a few cases where they do occur, particularly in odd-mass chains far from neutron sub-shell closures.

An example is  $^{103}\text{Y}$ , which has a ground-state threshold  $E_{\text{thr,gs-gs}} = 10.83$  MeV, while the electron capture daughter  $^{103}\text{Sr}$  has  $E_{\text{thr,gs-gs}} = 13.39$  MeV. For non-zero temperature an Urca process can occur for a small range of  $\mu_e$  where both  $^{103}\text{Y}$  electron capture and  $^{103}\text{Sr}$   $\beta^-$  decay are fast compared to the accretion timescale. Using the electron capture and  $\beta^-$  decay rates from our QRPA model we estimate that only a few Urca cycles can occur for the peak temperature and accretion rate considered here. With each cycle releasing about  $0.135$  MeV per nucleus, we find for this particular case an ad-

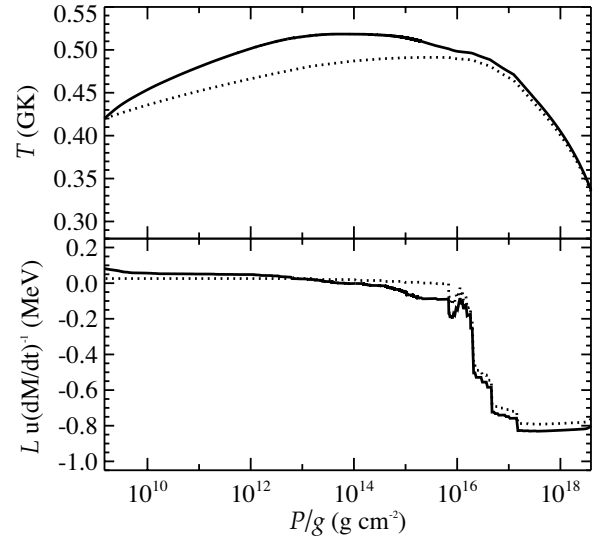


FIG. 5.— Temperature (*top*) and luminosity (*bottom*) in the neutron star crust, as functions of  $P/g$ , for a crust composed of heavy rp-process nuclei (*solid lines*). For comparison we also show the temperature and luminosity (*dotted lines*) obtained using the crust composition and heating from Haensel & Zdunik (2003). We multiply the luminosity by  $m_u/\bar{M}$  so that the plotted quantity is in energy per accreted nucleon.

ditional neutrino energy loss of  $0.3 \text{ keV u}^{-1}$  (using the abundance in the mass 103 chain  $Y_{103} \sim 7 \times 10^{-4}$ ). Even if such processes occur for about a handful of transitions, the total neutrino energy loss from this effect will be negligible.

The rate of energy loss from neutrinos through this mechanism is obviously very sensitive to temperature; taking a logarithmic derivative of the rate for the pre-threshold capture suggests that the neutrino loss rate is  $\propto T^7$ . For the specific case considered here, the rate is so small that the contribution from this process is negligible for  $T \lesssim 8 \times 10^8$  K. It would be interesting to explore this process in more detail with accurate electron capture and  $\beta^-$  rates for a range of temperatures and accretion rates.

### 3.2.2. Superburst ashes

The previous calculation described the evolution of  $^{12}\text{C}$ -poor ashes produced during an rp-process in an X-ray burst. For accreting neutron stars that exhibit superbursts, which typically ignite at a density  $\lesssim 10^9 \text{ g cm}^{-3}$  (Cumming et al. 2006), the burning during the superburst sets the initial crust composition rather than the X-ray burst. The composition in the region between the H/He burning shell and the carbon burning shell is also not well-described by X-ray burst ashes, as they do not contain sufficient amounts of  $^{12}\text{C}$  to ignite superbursts. A better estimate for the initial composition in superburst systems might therefore be the ashes of *stable* hydrogen and helium burning, which do contain sufficient amounts of carbon at the accretion rates considered here (Schatz et al. 2003b). We therefore perform a second calculation, in which we use as an initial composition the ashes of steady-state hydrogen and helium burning at the accretion rate of  $0.3\dot{M}_{\text{Edd}}$  (Schatz et al. 2003b). This ash consists mainly of  $^{52}\text{Cr}$  (36% by mass),  $^{12}\text{C}$  (8% by mass),  $^{57}\text{Co}+^{57}\text{Fe}$  (8% by mass together),  $^{58}\text{Ni}$  (6% by mass), and  $^{60}\text{Ni}$  (5% by mass). We then assume a composition change at  $\mu_e = 4.3$  MeV ( $\rho = 1.7 \times 10^9 \text{ g cm}^{-3}$ ) to the superburst ashes of Schatz et al. (2003a). The superburst ash consists mainly of  $^{66}\text{Ni}$  (35% by

mass),  $^{64}\text{Ni}$  (15% by mass), and  $^{60}\text{Fe}$  (14% by mass).

The electron captures on steady-state rp-process ashes in the region  $0.45 \text{ MeV} < \mu_e < 4.3 \text{ MeV}$  result in  $24 \text{ keV u}^{-1}$  of heating, while the superburst ashes deposit  $32.5 \text{ keV u}^{-1}$  in the range  $4.3 \text{ MeV} < \mu_e < 14 \text{ MeV}$ . This latter heat deposition is slightly greater than half that deposited by the X-ray burst ashes in the same range of  $\mu_e$ . For  $\mu_e < 18.5 \text{ MeV}$  the energy deposition is dominated by just two transitions,  $^{66}\text{Ni} \rightarrow ^{66}\text{Fe}$  at  $\mu_e = 9.2 \text{ MeV}$  and  $^{66}\text{Fe} \rightarrow ^{66}\text{Cr}$  at  $\mu_e = 15.1 \text{ MeV}$ . In both these transitions the second electron capture step populates relatively high lying excited states at 3.6 and 2.9 MeV respectively, hence the relatively large heat release. The fact that fewer transitions contribute to the heating is not unexpected as the composition is more homogeneous than in the case of the rp-process ashes. At  $\mu_e \gtrsim 18.5 \text{ MeV}$  there is strong heating ( $34 \text{ keV u}^{-1}$ ) from both neutron-induced reactions and the capture  $^{64}\text{Cr} \rightarrow ^{64}\text{Ti}$ .

### 3.2.3. Dependence on composition

The different heating obtained for rp-process and superburst ashes illustrates clearly that the composition matters, when one accounts for electron captures into excited states. The excitation energies populated by allowed Gamow-Teller transitions depend strongly on nuclear structure, in particular on shell and sub-shell closures. Figure 6 shows for each parent nucleus the main excitation energy of the electron capture daughter nucleus. Clearly there are huge differences with particularly high excitation energies occurring near the shell closures. If the initial composition has a large fraction of its nuclei that will go through a region of high excitation energy, then particularly large heat deposition will occur. Away from the shell closures, nuclear deformation tends to fragment Gamow-Teller strength and suitable transitions are more likely to occur at lower excitation energies.

Although the  $(\gamma, n)$  reactions are suppressed where  $S_n < \hbar\omega_{p,e}$ , we note that any neutron-induced reaction sequences and their energy release will also depend strongly on composition. For example, in a mix of nuclei,  $(\gamma, n)$  reactions will tend to occur at shallower depths in  $A$ -chains that reach low neutron separation energies first (usually only one nucleus exists in a mass chain at a particular depth and the heavier, odd-mass chains lose neutrons first). In addition to the neutron donors, if suitable neutron-accepting nuclei are available in other mass chains at the time the neutrons are released, then a net release of heat can occur as the composition becomes more neutron bound. Depending on the composition, there will be a depth where neutron emission would occur without suitable neutron capture targets available. From there on an appreciable neutron abundance would build up. Even if  $(\gamma, n)$  reactions are completely suppressed such effects might occur once the first  $A$ -chains have reached neutron drip deeper in the crust. In addition, these neutron capture and  $(\gamma, n)$  reactions will move material to neighboring  $A$ -chains with different electron capture thresholds and  $\beta$ -decay  $Q$ -values and thereby induce additional weak reactions that otherwise would not have occurred at that depth.

### 3.3. An Approximate Model

To explore the composition dependence further, and to disentangle the impact of the various differences to previous models more clearly, we present a simplified model of the heating in the neutron star crust. In the spirit of some previous studies (Haensel & Zdunik 1990, 2003) we limit the model to

electron captures only (no neutron reactions), we assume that electron captures proceed immediately when  $\mu_e$  reaches or exceeds the threshold, and we assume that 75% of the electron capture transition energy is released in form of neutrinos. In contrast to previous work, we do take into account that electron captures populate excited states in the daughter nuclei. We make the simplifying assumption that only the lowest lying daughter state with significant strength is populated.

To test this model we calculate the heat release as a function of depth for our initial rp-process ashes and compare the result (*dotted line*, Figure 4) with the full network calculations for the rp-process burst ashes. Up to  $\mu_e \approx 14 \text{ MeV}$  there is mostly good agreement. The slight offset at low  $\mu_e$  is because the tabulation of the approximate model does not include captures at  $\mu_e < 2.0 \text{ MeV}$ . The differences at higher  $\mu_e$  are due to heating from neutron-induced reactions in the reaction network. For captures onto nuclei for which  $\mu_e \gg E_{\text{thr}}$  our approximate model also underestimates the fraction of heat carried off by the neutrino. Nevertheless, this approximate model provides a good estimate of the crustal heating.

To explore the composition dependence further, Figure 7 maps out the heating, per nucleon, deposited in the crust as a function of mass number  $A$  at each depth  $\mu_e$ , if the crust were composed of a single species with that mass number. For each  $A$ , we start with an initial isotope  $(Z, A)$  that is stable at the low-density boundary. We then use our approximate model to trace the heat deposition from successive electron captures with increasing  $\mu_e$ . The area of each dot indicates the heat deposited in the crust for each transition, and its vertical location indicates the  $\mu_e$  at the transition. The largest heat deposit is for  $A = 38$  at  $\mu_e = 17.3 \text{ MeV}$  with  $Q = 0.28 \text{ MeV u}^{-1}$ . For this calculation we only include electron captures in the region  $\mu_e < 20 \text{ MeV}$ .

In Figure 7 we also show the total deposited heat as a function of the mass number  $A$  for each mass chain (*top panel, black histogram*). The greatest crustal heating would occur for a composition dominated by  $A = 38$  or  $A = 42$  with heat deposition reaching  $0.45 \text{ MeV u}^{-1}$ . Heavy ashes tend to release less energy per nucleon as excitation energies are similar but the nuclei include more nucleons. Nevertheless, shell effects lead to large heating for  $A = 68\text{--}91$  with particularly high values for  $A = 70, 84, 86, \text{ and } 88$ . In systems without superbursts, rp-process ashes rich in such nuclei would lead to a hotter crust. Superburst ashes in the mass range  $A = 60\text{--}66$  and the rp-process ashes dominated by  $A = 104$  are less favorable for heating the crust.

For comparison, we also show the heat deposition calculated with the same method but assuming ground-state transitions only (*grey histogram*). Taking into account realistic transition energies for electron captures leads to a dramatic increase in heat deposition that is strongly composition dependent.

## 4. SUPERBURST IGNITION

As shown in Figure 4, the heat deposited in the outer crust is roughly 4 times greater than that computed in an approach that neglects captures into excited states. This greater heat release in the outer crust raises the temperature (Fig. 5) in the region where  $^{12}\text{C}$  would unstably ignite, and hence one signature of this enhanced heating is a reduction in the ignition column depth  $y_{\text{ign}}$  for superbursts. We calculate the column depth  $y_{\text{ign}}$  for unstable carbon ignition using the composition from steady-state rp-process burning and the superburst

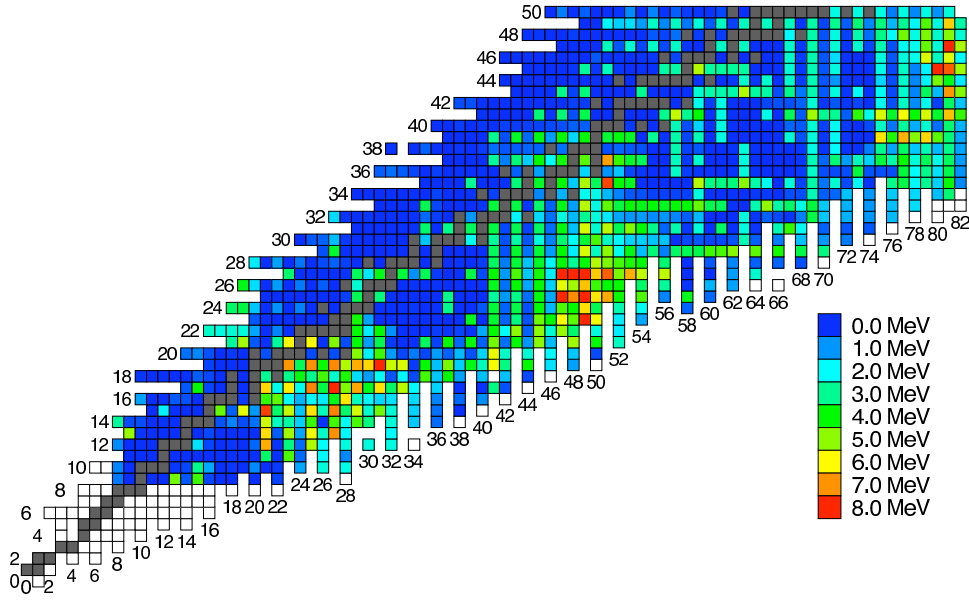


FIG. 6.— For each parent nucleus we show the excitation energy of the dominant state in the daughter nucleus populated by electron capture. Electron capture sequences passing through regions with high excitation energies in the daughter will result in increased heat deposition.

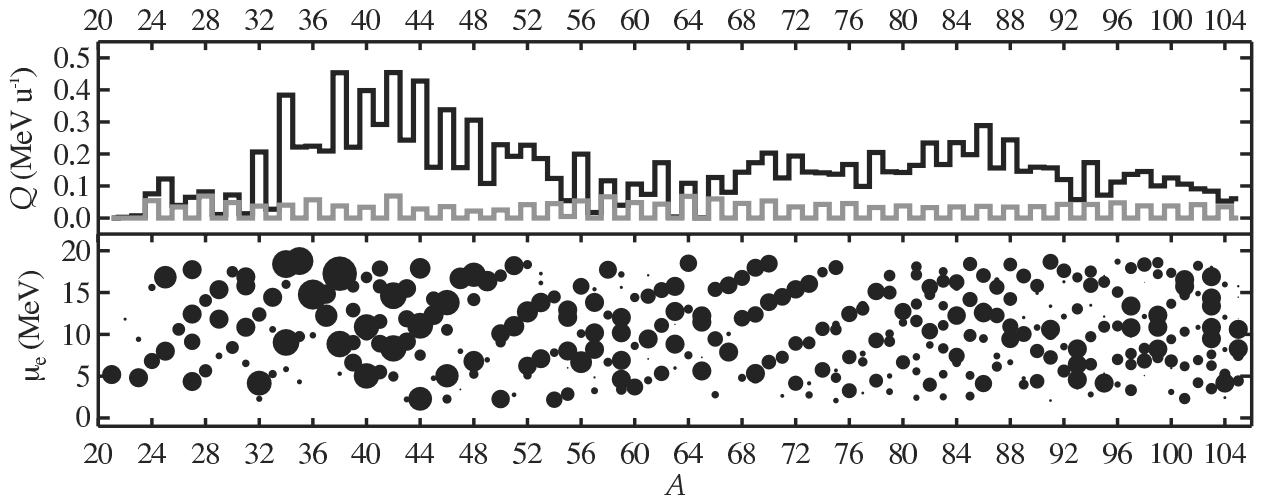


FIG. 7.— Electron captures in the outer crust. The mass number  $A$  is along the horizontal axis; accretion pushes the fluid to greater  $\mu_e$ , which is upward on the bottom panel. Each dot on the bottom plot indicates the heat deposited into the crust by a given mass chain at that  $\mu_e$ , with the area of each dot being proportional to the amount of heat deposited. The top panel shows the total heat deposited in the crust (*black histogram*) for that mass chain, as described in 3.3. In particular, the heat released by  $(n, \gamma)$  reactions is neglected. For comparison, the heat that would be deposited if all transitions were ground-state-to-ground-state is also shown (*top, grey histogram*).

ashes as described in § 3.2.2. These ashes do contain  $^{12}\text{C}$  at mass fraction  $X(^{12}\text{C}) = 0.08$ . After solving for the thermal profile (Fig. 8), as described in § 2, we locate the ignition column  $y_{\text{ign}}$  using the one-zone stability analysis described in Cumming & Bildsten (2001). Our reaction rate is taken from Caughlan & Fowler (1988), with screening according to the prescription of Ogata et al. (1993). These results overestimate the enhancement of the reaction rate (Ogata 1997; Yakovlev et al. 2006). For the case of  $^{12}\text{C} + ^{12}\text{C}$  fusion and the densities of interest, we find that our ignition depths increase by  $\lesssim 20\%$  when using the screening term indicated by Yakovlev et al. (2006).

These ignition points are marked (*squares*) on Figure 8. The ignition column for the four models, from shallowest to deepest, are  $y_{\text{ign}}/(10^{12} \text{ g cm}^{-2}) = 3.7, 4.8, 4.9,$  and  $6.3$ . The corresponding recurrence times are  $t_{\text{rec}} = y_{\text{ign}}/\dot{m} = 5.6, 7.2, 7.4,$

and  $9.5$  yr. The change in outer crust composition from a single mass  $A = 56$  with only captures into ground state to a realistic mixture of rp-process and superburst ashes shortens the recurrence time by about 20%. The increase in temperature at  $y \lesssim 10^{12} \text{ g cm}^{-2}$  is much less dramatic between the two crust models. This is due in part because both the steady-state rp-process and the superburst produce mass chains that are devoid of captures at low  $\mu_e$  (cf. Fig. 7).

We use the approximate model (§ 3.3) to investigate how the ignition depth depends on the heating in, and hence composition of, the outer crust. For each mass chain, we computed a thermal profile for a crust composed of that nuclide. As shown in Figure 9, there is a wide variety in temperatures in the outer crust. The cases shown have the same boundary conditions as described in § 2. As Figure 7 shows there is a wide variation among the different  $A$ -chains in the amount of heat deposited and the deposition depth, which leads to a

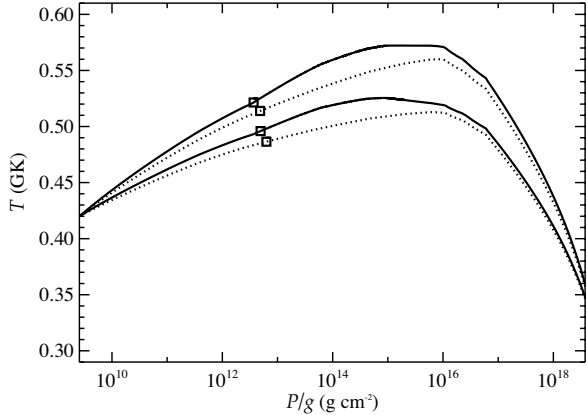


FIG. 8.— Thermal profiles for crusts with an outer layer of *steady state* rp-process ashes, an outer crust composed of superburst ashes, with heating computed either by our network calculations (*solid lines*) or according to the model of Haensel & Zdunik (1990, *dotted lines*), and an inner crust computed from the model of Haensel & Zdunik (1990). The upper set of curves have the Cooper-pair neutrino emissivity suppressed. The column where  $^{12}\text{C}$  unstably ignites is indicated for each solution (*squares*).

sizable difference in temperature at column  $y \sim 10^{12} \text{ g cm}^{-2}$ .

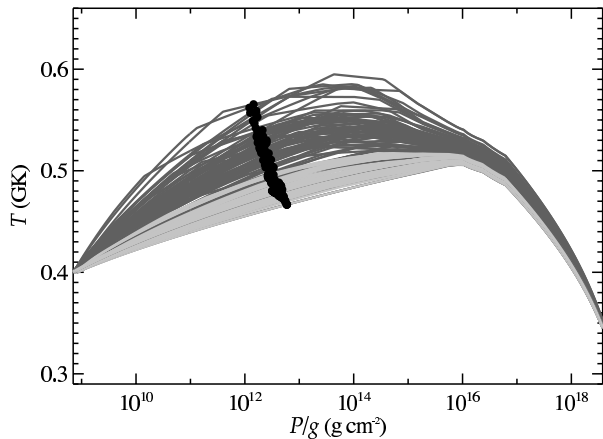


FIG. 9.— Temperature in the neutron star crust for mass chains with  $A = 21\text{--}105$ . We show two models, one with captures into excited states included (*dark grey lines*) and one with only ground-state captures (*light grey lines*). In each case we set  $\dot{M} = 3.0 \times 10^{17} \text{ g s}^{-1}$  and impose the same boundary conditions. For comparison, we also show for each model where  $^{12}\text{C}$  would unstably ignite (*dots*).

To follow how this variation in temperature affects the ignition depth, we then computed where a mixture of the the crust material and  $^{12}\text{C}$ , with  $X(^{12}\text{C}) = 0.2$ , would unstably ignite. The ignition points are shown in Figure 9 (*black dots*), and we plot  $y_{\text{ign}}$  as a function of the mass chain  $A$  in Figure 10 (*black histogram*). For comparison, we also show the ignition depth computed when captures into excited states are neglected (*grey histogram*). There is a general trend that the ignition depth decreases with increasing  $A$ , even for the case with no excitation energy. This is a consequence of two factors. First, the electron density at a given column (pressure) increases slightly with  $\langle Z \rangle$  to offset the negative Coulomb contribution to the pressure. Second, the timescale for a temperature perturbation at a column of  $10^{12} \text{ g cm}^{-2}$  to diffuse away increases by a factor of  $\approx 3$  as  $A$  increases from 21 to 105. Both of these effects act to reduce the column needed to unstably ignite a  $^{12}\text{C}$ -enriched plasma. This variation with  $A$

is probably exaggerated somewhat, because we did not self-consistently solve the thermal profile with the admixture of  $^{12}\text{C}$  at  $y < y_{\text{ign}}$ , which would reduce the disparity in the mean value of  $Z$  and  $A$  among mass chains. Nevertheless, this exercise demonstrates how the superburst ignition depth depends on the makeup of the ashes of H and He burning, and the importance of correctly treating the underlying nuclear physics of the crust. The range of ignition times is more consistent with the fitted recurrence times (Fig. 10, *thin dotted lines*) of Cumming et al. (2006, Table 1) when captures into excited states are included, but is still not shallow enough to accommodate all of the inferred ignition depths. To reduce the ignition column further would require a reduction in the core neutrino emissivity below modified Urca, as suggested by Cumming et al. (2006).

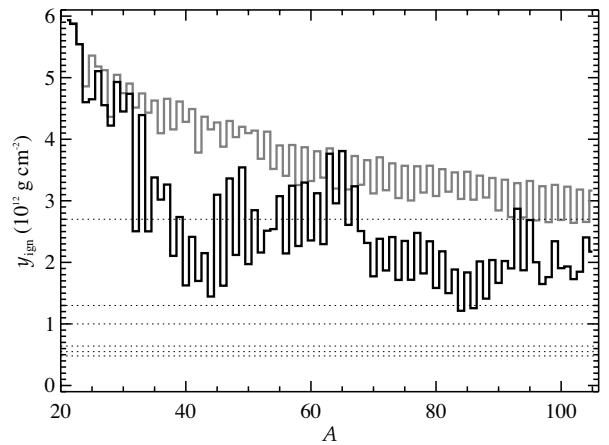


FIG. 10.— Carbon ignition depth  $y_{\text{ign}}$  for crusts composed of different mass chains  $A$ . The thermal profile is calculated using our approximate model. The difference in heating between the cases for which captures into excited states are included (*black histogram*) and neglected (*grey histogram*) are clearly evident. For comparison, we also show the fitted ignition depths according to Cumming et al. (2006, Table 1) (*thin dotted lines*).

If the Cooper-pairing neutrino emissivity were suppressed in the inner crust, then the ignition depth is decreased further (Fig. 11). As before, the inclusion of electron captures into excited states reduces the discrepancy between the calculated  $y_{\text{ign}}$  and those fitted from observations.

## 5. SUMMARY AND CONCLUSIONS

We show that allowing for electron captures into excited states drastically increases the heat deposited into the outer crust of accreting neutron stars. The fraction of the reaction energy carried away by neutrinos is sharply curtailed. We also find that the amount of heating in the crust is very sensitive to the initial composition forged during the burning of light elements in the neutron star envelope. This sensitivity is a consequence of the pronounced shell and sub-shell structure of neutron-rich nuclei, which can lead to drastic changes in shape, single-particle level structure, and electron capture strength distributions, even between nuclei of similar  $Z, A$ .

We have explored how this increased deposition affects the ignition depth, and hence the recurrence time, of superbursts. For a realistic composition—steady-state rp-process ashes overlying superburst ashes—the inclusion of the excited states decreases the ignition depth by about 20%. For the most optimistic case we consider, in which the neutrino emissivity

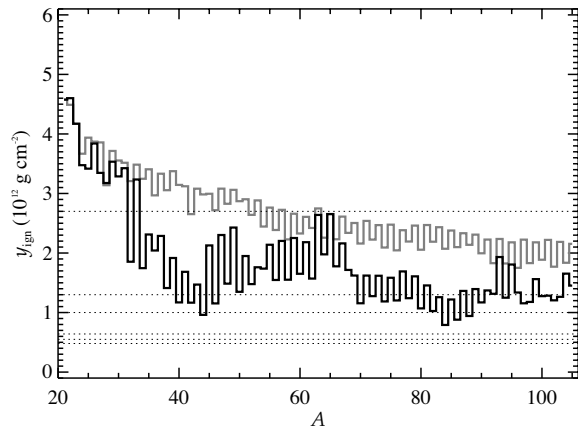


FIG. 11.— Same as Fig. 10, but for the Cooper-pairing neutrino emissivity suppressed.

from Cooper-pairing is suppressed, the ignition depth for accretion at 0.3 Eddington is  $y_{\text{ign}} = 3.7 \times 10^{12} \text{ g cm}^{-2}$ , closer to the value inferred from observations ( $y_{\text{ign}} = 5 \times 10^{11} - 2.7 \times 10^{12} \text{ g cm}^{-2}$ ; Cumming et al. 2006), although a significant discrepancy remains unless the core neutrino emissivity is reduced below the modified Urca rate.

To explore the variation of superburst ignition depths with composition, we have constructed an approximate model of the heating in the crust. Using this model and including the neutrino emissivity from paired neutrons, we find that at 0.3 Eddington the superburst ignition depth can be as low as  $1.3 \times 10^{12} \text{ g cm}^{-2}$  if the composition is dominated by nuclei with  $A = 40-44$  or  $82-86$ . The corresponding recurrence time for ignition at this depth, with the assumed accretion rate and neutron star parameters, is 2 yr. This is roughly consistent with the observations, without invoking any additional

physics. We are not aware, however, of a mechanism that would, for example, avoid the production of nuclei around  $A \approx 60$  dominating the superburst ashes.

Our results also indicate that crustal heating is very sensitive to the underlying nuclear physics. Reliable estimates of the structure of very neutron-rich nuclei up to  $A = 106$  are needed to constrain the lowest lying electron capture strength, which determines the heating from the deexcitation of excited daughter states. Nuclear masses are needed to determine reaction thresholds and neutron separation energies. Finally, masses,  $\beta^-$ -decay rates, and reaction rates for the proton and helium-induced reactions on very neutron deficient nuclei during hydrogen and helium burning in the  $\alpha p$ - and  $rp$ -processes are needed to accurately determine the initial composition. More work is also needed to extend our calculations into the inner crust to determine the heating there.

It is a pleasure to thank Lars Bildsten, Andrew Cumming, Dany Page, and Andrew Steiner for stimulating and fruitful conversations, and the referee for a careful and thorough reading of the text, which greatly improved the manuscript. We thank Friedel Thielemann for providing the network solver and Michelle Ouellette for contributing to the network code. This work is supported by the Joint Institute for Nuclear Astrophysics under NSF-PFC grant PHY 02-16783 and by NSF grant PHY 0110253. K. L. K. acknowledges support from Virtuelles Institut für Struktur der Kerne und nukleare Astrophysik (VISTARS) under HGF grant VH-VI-061. This work was partially carried out under the auspices of the National Nuclear Security Administration of the US Department of Energy at Los Alamos National Laboratory under Contract DE-AC52-06NA25396.

#### REFERENCES

- Ainsworth, T. L., Wambach, J., & Pines, D. 1989, *Phys. Lett. B*, 222, 173  
 Akmal, A., Pandharipande, V. R., & Ravenhall, D. G. 1998, *Phys. Rev. C*, 58, 1804  
 Becerril Reyes, A. D., Gupta, S., Kratz, K. L., Möller, P., & Schatz, H. 2006, in *Nuclei in the Cosmos IX*, ed. J. Cederkäll et al. (Trieste: SISSA)  
 Brown, E. F. 2000, *ApJ*, 531, 988  
 Brown, E. F. 2004, *ApJ*, 614, L57  
 Brown, E. F., Bildsten, L., & Chang, P. 2002, *ApJ*, 574, 920  
 Caughlan, G. R. & Fowler, W. A. 1988, *At. Data Nucl. Data Tables*, 40, 283  
 Cooper, R. L. & Narayan, R. 2005, *ApJ*, 629, 422  
 Cumming, A. & Bildsten, L. 2001, *ApJ*, 559, L127  
 Cumming, A. & Macbeth, J. 2004, *ApJ*, 603, L37  
 Cumming, A., Macbeth, J., in 't Zand, J. J. M., & Page, D. 2006, *ApJ*, 646, 429  
 Farouki, R. & Hamaguchi, S. 1993, *Phys. Rev. E*, 47, 4330  
 Frevert, L., Schöneberg, R., & Flammersfeld, A. 1965, *Z. Phys.*, 185, 217  
 Haensel, P., Kaminker, A. D., & Yakovlev, D. G. 1996, *A&A*, 314, 328  
 Haensel, P. & Zdunik, J. L. 1990, *A&A*, 227, 431  
 —. 2003, *A&A*, 404, L33  
 in 't Zand, J. J. M., Cornelisse, R., & Cumming, A. 2004a, *A&A*, 426, 257  
 in 't Zand, J. J. M., Cornelisse, R., Kuulkers, E., Verbunt, F., & Heise, J. 2004b, in *Proc. "X-Ray Timing 2003: Rossi and Beyond"*, ed. J. H. S. P. Kaaret, F. K. Lamb (Melville, NY: American Institute of Physics), in press (astro-ph/0407087)  
 Itoh, N., Hayashi, H., Nishikawa, A., & Kohyama, Y. 1996, *ApJS*, 102, 411  
 Itoh, N. & Kohyama, Y. 1993, *ApJ*, 404, 268  
 Jones, P. B. 2004, *Phys. Rev. Lett.*, 93, 221101  
 Kaminker, A. D., Pethick, C. J., Potekhin, A. Y., Thorsson, V., & Yakovlev, D. G. 1999, *A&A*, 343, 1009  
 Kuulkers, E. 2004, *Nucl. Phys. B Proc. Suppl.*, 132, 466  
 Kuulkers, E., in 't Zand, J., Homan, J., van Straaten, S., Altamirano, D., & van der Klis, M. 2004, in *X-ray Timing 2003: Rossi and Beyond*, ed. P. Kaaret, F. K. Lamb, & J. H. Swank (Melville, NY: AIP Press)  
 Lattimer, J. M. & Prakash, M. 2001, *ApJ*, 550, 426  
 Leinson, L. B. & Perez, A. 2006, *Phys. Lett. B*, 638, 114  
 Mackie, F. D. & Baym, G. 1977, *Nucl. Phys. A*, 285, 332  
 Möller, P., Nix, J. R., Myers, W. D., & Swiatecki, W. J. 1995, *At. Data Nucl. Data Tables*, 59, 185  
 Möller, P. & Randrup, J. 1990, *Nucl. Phys. A*, 514, 1  
 Negele, J. W. & Vautherin, D. 1973, *Nucl. Phys. A*, 207, 298  
 Ogata, S. 1997, *ApJ*, 481, 883  
 Ogata, S., Ichimaru, S., & Van Horn, H. M. 1993, *ApJ*, 417, 265  
 Page, D. & Cumming, A. 2005, *ApJ*, 635, L157  
 Pethick, C. J. & Ravenhall, D. G. 1998, in *Trends in nuclear physics, 100 years later*, ed. H. e. a. Nifenecker, Les Houches Session LXVI, 1996 (New York: Elsevier), 717  
 Pethick, C. J. & Thorsson, V. 1994, *Phys. Rev. Lett.*, 72, 1964  
 Rauscher, T. & Thielemann, F. 2000, *At. Data Nucl. Data Tables*, 75, 1  
 Sato, K. 1979, *Prog. Theor. Physics*, 62, 957  
 Schatz, H., Aprahamian, A., Barnard, V., Bildsten, L., Cumming, A., Ouellette, M., Rauscher, T., Thielemann, F.-K., & Wiescher, M. 2001, *Phys. Rev. Lett.*, 86, 3471  
 Schatz, H., Bildsten, L., & Cumming, A. 2003a, *ApJ*, 583, L87  
 Schatz, H., Bildsten, L., Cumming, A., & Ouellette, M. 2003b, *Nucl. Phys. A*, 718, 247  
 Schatz, H., Bildsten, L., Cumming, A., & Wiescher, M. 1999, *ApJ*, 524, 1014  
 Sedrakian, A., Muther, H., & Schuck, P. 2006, *ArXiv Astrophysics e-prints*  
 Strohmayer, T. E. & Bildsten, L. 2004, in *Compact Stellar X-ray Sources*, ed. W. Lewin & M. van der Klis (Cambridge: Cambridge University Press), 113

Strohmayer, T. E. & Brown, E. F. 2002, ApJ, 566, 1045

Timmes, F. X. & Swesty, F. D. 2000, ApJS, 126, 501

Tolman, R. C. 1939, Physical Review, 55, 364

Wijnands, R. 2001, ApJ, 554, L59

Yakovlev, D. G., Gasques, L. R., Afanasjev, A. V., Beard, M., & Wiescher,  
M. 2006, Phys. Rev. C, 74, 035803

Yakovlev, D. G., Kaminker, A. D., & Levenfish, K. P. 1999, A&A, 343, 650